ELSEVIER

Contents lists available at ScienceDirect

Journal of Materials Processing Tech.

journal homepage: www.elsevier.com/locate/jmatprotec





Amorphous interfacial microstructure and high bonding strength in Al-Fe bimetallic components enabled by a large-area solid-state additive manufacturing technique

F.C. Liu^a, P. Dong a,b,*, A.S. Khan , K. Sun^c, W. Lu^{b,c}, A. Taub^{b,c}, J.E. Allison^{b,c}

- ^a Department of Naval Architecture and Marine Engineering, University of Michigan, Ann Arbor, MI 48109, USA
- ^b Department of Mechanical Engineering, University of Michigan, Ann Arbor, MI 48109, USA
- ^c Department of Materials Science and Engineering, University of Michigan, Ann Arbor, MI 48109, USA

ARTICLE INFO

Associate Editor: Jingjing Li

Keywords:
Friction stir additive manufacturing
Friction stir welding
Dissimilar metals
Interfacial amorphization
Amorphization mechanism
Intermetallic compounds

ABSTRACT

There is a growing demand for the ability to manufacture large-scale aluminum-steel (Al-Fe) bimetallic components for realizing the enormous advantages of advanced multi-material structures which offers effective lightweighting and increasingly smart functionalities. The formation of brittle intermetallic compounds (IMCs) at the bonding interface has been the major barrier to safety-critical applications with existing manufacturing processes, including additive manufacturing techniques. This study showed that a combination of a novel modified friction stir additive manufacturing (M-FSAM) and pre-processing surface polishing of the stainless steel enables the formation of a relative homogenously distributed nanoscale amorphous layer along the bonding interface between the 6061 Al and the 304 stainless steel. As a result, the high interfacial bonding strength of 280 MPa was achieved. Compared to the existing friction stir welding/AM processes, M-FSAM enables a significant increase in tool traverse speed and a remarkable reduction in tool cost for Al-Fe bimetallic component manufacturing. The nanoscale amorphous layer consisted of a continuous O and Mg rich layer 10–20 nm in thickness and a discontinuous Al-Fe-Si layer 50–100 nm in thickness. The O and Mg rich layer consisted of an amorphous matrix with nanocrystalline precipitates while the Al-Fe-Si layer consisted of a q-glass with some degree of crystallinity. The formation mechanism of the unique Al-Fe interfacial microstructure was analyzed in detail in this study.

1. Introduction

Metal additive manufacturing (AM) can be defined as the process of joining metals layer by layer to make physical objects from 3D model data. By its nature, metal AM is a versatile and flexible digital manufacturing process and offers numerous benefits including highly customized products, less material waste, fewer parts to be assembled, and much more (Sames et al., 2016). Realizing the high potential of metal AM, the world's major industrialized countries are investing heavily in metal AM technologies as a key enabler for future manufacturing. The demand for large-scale dissimilar- or multi-metal AM technologies is increasing in various industrial sectors such as aerospace & defense, and power & energy, as suggested by Yu and Mishra (2021).

Among various potential dissimilar metal combinations, additive

manufacturing of aluminum-steel (Al-Fe) bimetallic components is of the greatest interest for many lightweight or multifunction structural applications as steel and aluminum alloys are the most widely used engineering metals. However, interlayer bonding between steel and aluminum alloy using today's fusion-based AM methods often results in the formation of brittle intermetallic compounds (IMCs) at the dissimilar metal interface. Cai et al. (2019) showed that the presence of thick IMCs at the Al-Fe interface can lead to brittle fracture at the interface and a reduction in bonding strength. This has limited the application of Al-Fe bimetallic components in critical load-bearing structures. Zhang and Bandyopadhyay (2021) fabricated 316 stainless steel and Al12Si aluminum alloy bimetallic structures with a compositionally graded transition using a directed energy deposition technology. FeAl, Fe₂Al₅, and FeAl₁₃ IMCs formed in the compositionally graded section. Defects of cracks or pores were observed at the interface region. The load-bearing

^{*} Corresponding author at: Department of Naval Architecture and Marine Engineering, University of Michigan, Ann Arbor, MI 48109, USA. *E-mail address:* dongp@umich.edu (P. Dong).

capability of the fabricated bimetallic structures was evaluated by a compression test rather than a tensile test.

Different from the traditional approaches which have been focused on mitigating IMCs at the Al-Fe bonding interface mainly through alloying and controlling the processing thermal history, Liu et al. (2020) recently demonstrated that the formation of thick IMCs at the Al-Fe interface can be suppressed by introducing a nanoscale amorphization layer at the interface, showing that rapid friction between an aluminum alloy and steel promoted a nanoscale interfacial premelting at an Al-Fe interface by triggering a nanoscale shear localization. The resulting strain rate within the shear localization layer can be sufficiently high to effectively suppress crystallization. The presence of the premelting metal layer at the Al-Fe interface facilitated a rapid diffusion of alloying elements into the premelting layer from surrounding alloys, forming an undercooled liquid alloy. The high shear strain rate within the undercooled liquid alloy was sustained until the interfacial temperature was low enough and the undercooled liquid alloy solidified into a layer of amorphous solid without relying on a super-high cooling rate. This process can be referred to as shear localization induced alloy amorphization (SLIAA) at the Al-Fe interface.

The aforementioned investigations by Liu et al. (2020) provided an in-depth understanding of the underlying shear localization mechanisms for suppressing detrimental IMCs at the Al-Fe interface. However, several challenges remain. For instance, how to reproduce the desirable local interfacial microstructure over the entire Al-Fe bonding interface during an AM process? Can such an AM process be implemented cost-effectively? Does such an amorphous interface offer adequate load-carrying capacity or damage tolerance?

Friction stir welding (FSW) is a promising method that has been studied widely for joining aluminum alloy and steels due to the relatively low heat input and reduced detrimental IMC. Watanabe et al. (2006) showed that a small amount of IMCs formed at the steel/aluminum interface and the region where the IMCs formed seemed to be the fracture path in the joints. Wang et al. (2019) demonstrated that a friction stir scribe tool was able to reduce heat input and the IMC layer thickness compared to traditional FSW for producing Al-Fe lap joints. Zhou et al. (2020) showed that friction surfacing assisted friction stir lap welding can increase the load-bearing capability by \sim 30% compared to conventional FSW Al/steel weld. Liu and Dong (2021) showed that even a slight penetration of the friction stir tool into the steel can cause the formation of IMC at the interface and reduce the load-bearing capability of the bonding interface. Therefore, novel technologies that can effectively prohibit the formation of detrimental IMCs need to be developed for increasing the bonding strength at the Al-Fe interface.

Friction stir additive manufacturing (FSAM) is a modification of the FSW process. Palanivel et al. (2015) demonstrated that the alloys fabricated by FSAM mainly consisted of refined wrought microstructure and thence excellent mechanical properties. They pointed out that the key benefits of FSAM as compared to fusion-based AM and ultrasonic AM include (1) the ability to fabricate large components, (2) faying surface contamination is not as vital as in ultrasonic AM, (3) the ability to bond dissimilar metals that are challenges for fusion welding and ultrasonic AM, high degree of reproducibility, etc.

The FSAM methods require a certain amount of penetration of the friction stir probe across the faying surface for achieving an interlaminar bonding (Fig. 1a). When dealing with Al-Fe combination with the steel

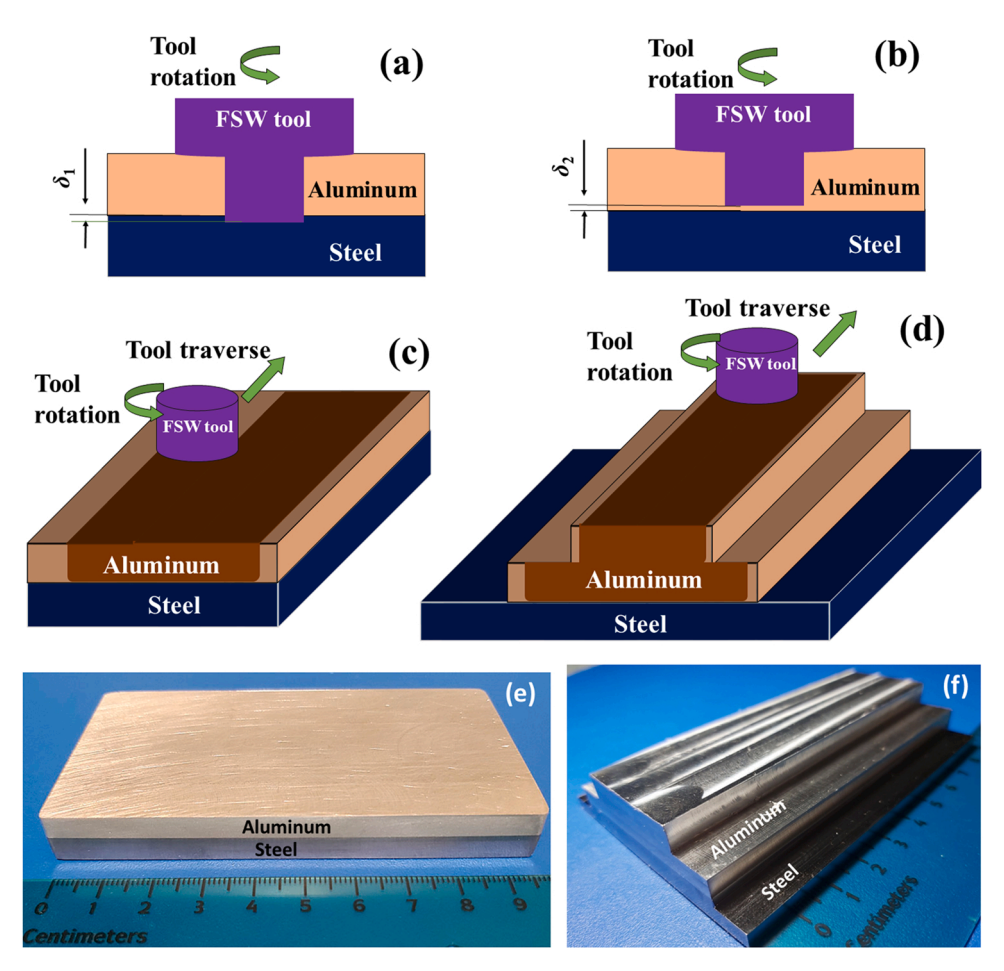


Fig. 1. Schematic illustration of the experimental setup of (a) FSAM with penetration of the stir probe into the steel and (b) M-FSAM with a distance between the stir probe and the steel. Concept of M-FSAM of large-scale Al-Fe bimetallic components: (c) two layers components and (d) three layers components. Typical Al-Fe bimetallic components produced by M-FSAM: (e) two layers components and (f) three layers components.

as the bottom substrate, FSAM needs to use expensive stir tools made of hard ceramic or refractory alloys. Since the friction and the coupled thermomechanical effect between the stir probe and the steel caused rapid tool wear and cracking development, the stir tools need to be replaced often in engineering applications, resulting in a high manufacturing cost. Liu et al. (2022) developed a modified FSAM (M-FSAM) which strategically positions the stir probe in the aluminum alloy at a short distance from the steel faying surface (Fig. 1b). They demonstrated that M-FSAM can be a potential method to introduce SLIAA at the Al-Fe interface. The M-FSAM not only suppressed the formation of IMC at the Al-Fe interface but also eliminated the need for expensive stir probes made of ceramic or refractory alloys, making it suitable for the cost-effective production of large-scale bimetallic components in this study (Fig. 1c and d).

It should be noted that the available investigations completed by Liu et al. (2022) have not been able to produce a continuous nanoscale amorphous layer at the entire Al-Fe interface. As a result, the efficacy of interfacial bonding strength and the robustness of M-FSAM in producing stronger Al-Fe bimetallic components remain to be demonstrated and understood. This issue will be addressed in this paper.

From the viewpoint of the interfacial material flow field, a reduced steel surface roughness should be desirable for generating and maintaining homogeneous friction between the deposited aluminum and the steel substrate along the entire bonding interface for achieving a continuous nanoscale amorphous layer and therefore a high bond strength. This will be substantiated as a result of this study. In addition to the steel surface roughness, process parameters, and local alloying effects on the formation of the nanoscale amorphous layer at the Al-Fe interface were also investigated. The advantages and robustness of the M-FSAM for producing stronger Al-Fe bimetallic components were demonstrated with experimental results. The excellent bonding strengths achieved in this study were shown to be a result of the formation of the nanoscale amorphous layer which consists of a continuous O and Mg rich layer 10-20 nm in thickness and a discontinuous Al-Fe-Si q-glass 50-100 nm in thickness. The formation mechanism of the unique Al-Fe interfacial microstructure was analyzed in detail in this study.

2. Materials and methods

A number of Al-Fe bimetallic components consisting of 6.35 mm thick 6061-T651 aluminum alloy sheets and 6.35 mm thick 304 stainless steel sheets were produced by the M-FSAM method. The chemical composition and mechanical properties of 6061-T651 Al and 304 steel were added in Tables 1 and 2. All the aluminum alloy sheets and stainless steel sheets were polished to a USA No. 8 mirror finish (Ra: $\sim\!0.15~\mu m$). The polished side of the sheets was protected by a plastic film, which was peeled off just before the M-FSAM experiments. The faying surfaces of the steel and aluminum alloy were cleaned using ethanol before the M-FSAM experiments. All the M-FSAM tools used in this study were made of H13 tool steel. These tools have a shoulder diameter of 18 mm, a probe diameter of 8 mm, and a probe length of 5.9 mm. The shoulder penetration is 0.4 mm for all the processes investigated in this study. The rotation rates and traverse speed of the tool were selected as control variables for investigation.

Miniature tensile test specimens were removed from the Al-Fe bimetallic components using water jet and electron discharge machining for evaluating the effects of processing conditions on the mechanical properties of the bimetallic components. The Al-Fe bonding

interface was located in the middle of the miniature tensile samples which have a gauge length of 2.5 mm, a gauge width of 1.4 mm, and a gauge thickness of 1.0 mm. Tensile tests using the miniature tensile samples were completed using an Instron 3366 testing machine at a crosshead speed of 0.1 mm/min. The fracture surfaces of the test samples were analyzed using a TESCAN MIRA3 FEG scanning electron microscope (SEM) at an accelerating voltage of 10 kV.

The samples for bonding interface analysis were mechanically polished from P240 sandpaper down to diamond polishing paste of 1 μm . The polished samples were analyzed using a TESCAN MIRA3 FEG SEM at an accelerating voltage of 30 kV. Thin foils across the Al-Fe bonding interface were removed by a focused ion beam (FIB) installed on an FEI Helios Nanolab 650 for transmission electron microscope (TEM) analysis. The chemical quantification analysis across the bond interface was performed using a Thermo-Fisher Talos F200X G2 TEM, which was equipped with 4 in-column X-ray silicon drift detectors with unique cleanliness, offering accurate chemical quantification. The TEM was operated at 200 kV in STEM mode using a spot size of 3 that gave a higher beam current over the regular imaging settings. The EDS mapping was performed using Velox software with the data collected for 90 min. High-resolution scanning transmission electron microscope (HR-STEM) analysis was performed using a double aberration-corrected analytical TEM (JEOL 3100R05) at an accelerating voltage of 300 kV.

3. Results

3.1. Fabrication of Al-Fe bimetallic components using M-FSAM

Liu et al. (2020) showed that the key to promoting premelting and alloy amorphization at an Al-Fe interface is to introduce sufficient friction between the aluminum alloy and steel below the melting point of the aluminum alloy. Guided by this principle, the end surface of the stir probe was strategically placed 0.05 mm above the faying surface of 304 stainless steel during all the M-FSAM experiments since 0.05 mm was found to be optimal by thorough testing. This operation allows the aluminum alloy underneath the stir probe to be driven to rub against the steel faying surface for promoting interfacial premelting and shear localization.

To demonstrate the potential of the M-FSAM for fabricating large-scale Al-Fe bimetallic components, multiple-pass M-FSAM was developed to produce two-layer and three-layer Al-Fe bimetallic components. The M-FSAM parameter of 1000 rpm and 600 mm/min was used for the fabrication of the bimetallic components. Two Al-Fe bimetallic components that were removed from the Al-Fe bimetallic components produced by M-FSAM were shown in Fig. 1e and f.

3.2. Interfacial microstructure

Fig. 2 shows the interfacial microstructure of the bimetallic components of 6061 aluminum alloy and polished 304 stainless steel produced by M-FSAM at 1000 rpm and 600 mm/min. Since polished 304 stainless steel was used, the bimetallic component of 6061 aluminum alloy and the polished 304 stainless steel have a flatter bonding interface (Fig. 2a). Only a few small scratches created by the polishing process (shallower than 300 nm) were observed at relatively higher magnification (Fig. 2b). A discontinuous transition layer thinner than 100 nm was the dominant interfacial microstructure at the flat bonding interface (Fig. 2c). Such an Al-Fe interfacial microstructure is quite different from those produced

Table 1Chemical composition and mechanical properties of 6061-T651 Al.

Chemical composition (wt%)									Mechanical properties			
Mg	Si	Fe	Cu	Cr	Zn	Ti	V	Other	Al	UTS (MPa)	YS (MPa)	Elongation (%)
1.1	0.73	0.50	0.29	0.08	0.14	0.02	0.01	0.02	Bal.	330	296	13.8

Table 2 Chemical composition and mechanical properties of 304 steel.

Chemical composition (wt%)										Mechanical properties			
Cr	Ni	Mn	Cu	Mo	С	N	P	S	Fe	UTS (MPa)	YS (MPa)	Elongation (%)	
18.18	8.02	1.83	0.54	0.39	0.01	0.01	0.03	0.003	Bal.	639.8	345.2	48.9	

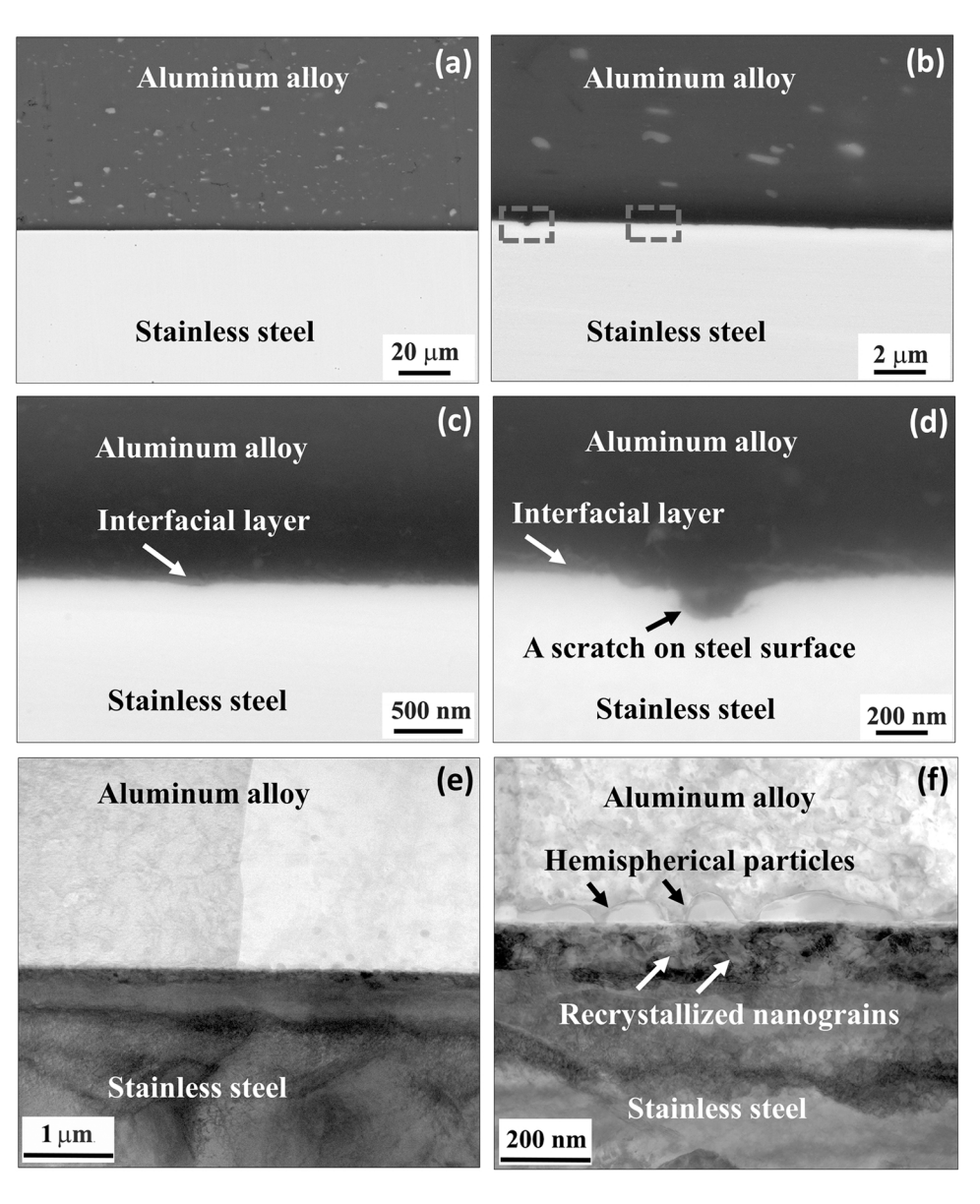


Fig. 2. SEM Backscatter electron image of the interface of the bimetallic components of 6061 aluminum alloy and 304 stainless steel produced at 1000 rpm and 600 mm/min: (a) low magnification image, (b) intermediate magnification image, (c) right red rectangle in (b), and (d) left red rectangle in (b). STEM brightfield (BF) images: (e) low magnification image showing a generally uniform interfacial microstructure, (f) high magnification image showing interfacial details. Note: arrows pointing to amorphous regions.

by other welding or additive manufacturing methods in which the interfaces were often dominated by IMCs (Wang et al., 2019). Fig. 2d shows that a surface scratch from the original polished stainless steel was filled by aluminum alloys after M-FSAM and no cavity defect was observed at the bottom of the scratch.

To characterize more details of the thin transition layer, TEM samples were extracted from the smooth bonding interface of 6061 aluminum alloy and polished 304 stainless steel produced by M-FSAM at 1000 rpm and 600 mm/min. Fig. 2e shows that the top layer of the polished stainless steel contained a high density of dislocation and some recrystallized nanograins. Such a microstructure should be associated with the combination of local plastic deformation caused by the surface polishing and the temperature elevation during M-FSAM. An interesting phenomenon is that a discontinuous interlayer consisting of a series of

hemispherical particles that were 50–100 nm in thickness and 100–300 nm in length formed at the Al-Fe interface (Fig. 2f). These hemispherical particles were mainly located within the 6061 aluminum alloy and were attached to the stainless steel faying surface.

Fig. 3 shows the distribution of alloying elements around the Al-Fe interface. Special care was taken during both the sample preparation stage and the analysis stage to make the electron beam paralleled to the bonding interface to the highest degree to minimize the effect of 3D space on the 2D image. The following phenomena were observed. First, the hemispherical particles contained less Al than the adjacent aluminum alloy substrate. Second, the alloying elements of Fe, Ni, Cr, and Mn from the 304 stainless steel were present in the hemispherical particles. Third, the hemispherical particles contained a remarkably higher concentration of Si element than either the adjacent stainless

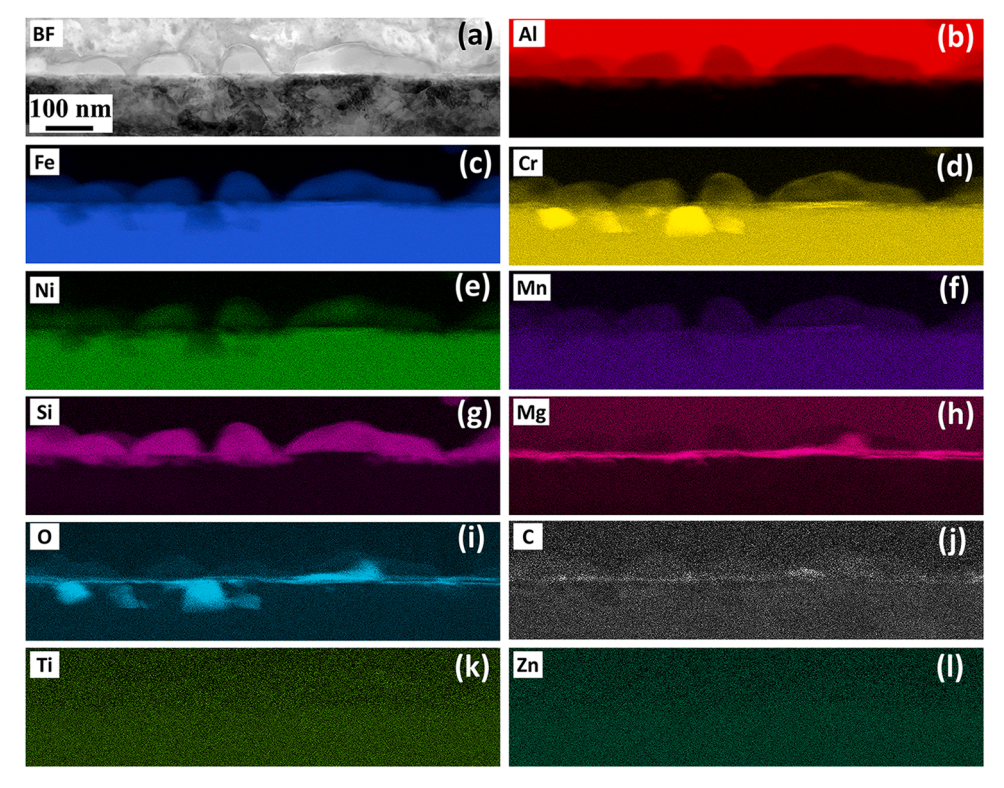


Fig. 3. (a) STEM BF image and X-ray energy-dispersive spectroscopy (EDS) elemental maps of (b) Al, (c) Fe, (d) Cr, (e) Ni, (f) Mn, (g) Si, (h) Mg, (i) O, (j) C, (k) Ti and (I) Zn, respectively.

steel or the adjacent aluminum alloy. Fourth, an Mg-depletion zone formed in the hemispherical particles, and an Mg-rich zone formed along the stainless-steel faying surface. Fifth, the Mg-rich zone contained a higher concentration of O and C elements than the matrix of the stainless steel and aluminum alloy. Sixth, no aggregation of Ti and Zn elements was detected around the bonding interface.

The distribution of the alloying elements across the bonding interface was quantitively analyzed at two representative locations: one is the Al-Fe interface that is free of hemispherical particles (Fig. 4a), and another is the Al-Fe interface that has an adjacent hemispherical particle (Fig. 4b). Both Figs. 3 and 4 show that the Al-Fe interface contained a remarkably higher concentration of O and Mg than the surrounding

areas, suggesting the formation of an O and Mg rich layer at the Al-Fe interface. The O and Mg rich layer was also detected at the interface that has a nearby hemispherical particle (Fig. 4b). These results are consistent with the element distribution in Fig. 3, which shows that a continuous O and Mg rich layer 10–20 nm in thickness formed at the faying surface of stainless steel. Fig. 4b shows a plateau of Al, Fe, Si, O, and Cr at the location of the hemispherical particle, suggesting that these alloying elements were distributed homogenously within the hemispherical particle. The average chemical composition of the hemispherical particles was summarized in Table 3, showing that the hemispherical particles were dominated by Al, Fe, and Si, elements and contained a low content of O, Cr, Ni, C, and Mg alloying elements.

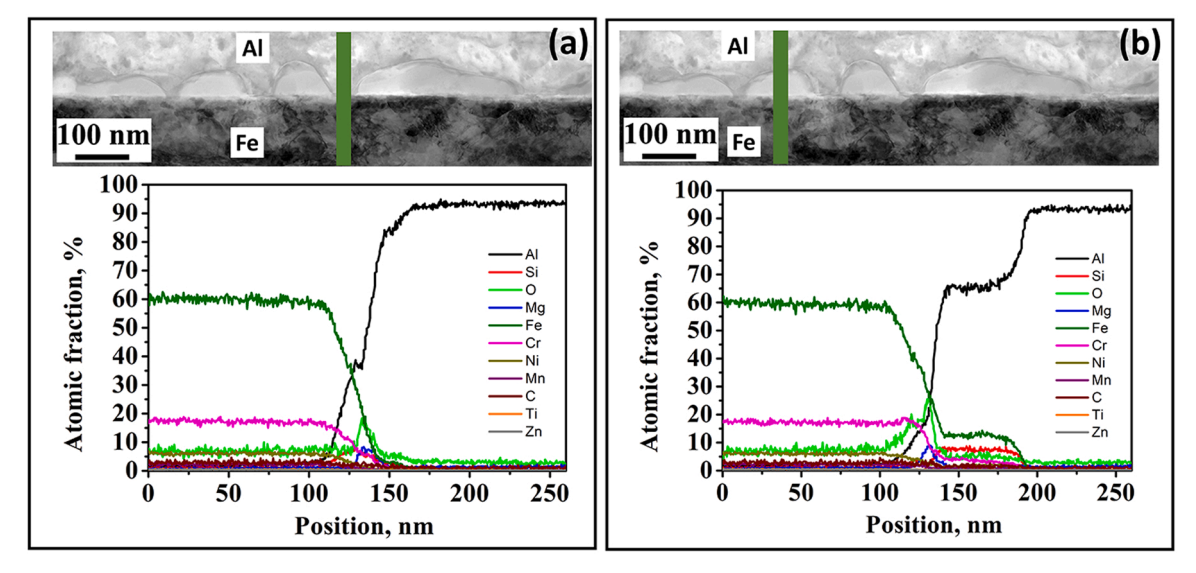


Fig. 4. EDS line profiles across the Al-Fe interface at the location (a) free of hemispherical particles and (b) with hemispherical particles, respectively.

Table 3Chemical composition of the amorphous particles (wt%) at Al-Fe interface.

Elements	Al	Fe	Si	0	Cr	Ni	С	Mg	Mn	Ti	Zn
at%	65.0	13.1	7.41	5.30	3.34	1.83	1.56	1.09	0.72	0.25	0.20
wt%	56.2	21.2	6.85	2.73	6.45	3.22	0.63	0.78	1.43	0.35	0.36

According to the TEM analysis above, the microstructure distribution around the Al-Fe interface can be schematically illustrated in Fig. 5 for further local analysis. The interfacial microstructure can be divided into a continuous O and Mg rich layer and a discontinuous Al-Fe-Si layer. The O and Mg rich layer formed directly on the stainless-steel faying face while the discontinuous Al-Fe-Si layer was located between the O and Mg rich layer and the aluminum alloy substrate.

To investigate the microstructure details of each layer at the Al-Fe interface and the connection between the layers, high-resolution scanning TEM (HR-STEM) was applied to analyze the microstructure at the interface (Fig. 6). Fig. 6a and e suggest that atomic-level bonding was achieved at the interfaces between the aluminum alloy substrate, the Al-Fe-Si layer, the O and Mg rich layer, and the stainless steel substrate. No large void-like defect was observed at any of the interfaces. Some degree of lattice fringes appeared to be dimly visible at some locations within the Al-Fe-Si layer (Fig. 6a). No nanocrystal precipitates were detected within the Al-Fe-Si layer (Fig. 6c). A fast Fourier transform (FFT) analysis of the Al-Fe-Si layer shows a combination of a halo feature and some sharp spots in the FFT pattern (Fig. 6d), suggesting that the Al-Fe-Si layer was an amorphous solid with some degree of crystallinity.

The FFT pattern obtained from the O and Mg rich layer also shows a combination of a halo feature and some sharp spots (Fig. 6f). Different from the Al-Fe-Si based layer, nanocrystal precipitates less than 5 nanometers in diameter were observed within the O and Mg rich layer (Fig. 6e), suggesting that the O and Mg rich layer can be treated as a layer of amorphous-crystalline nano-composite.

Fig. 7 shows the atomic distribution of the aluminum alloy adjacent to the Al-Fe interface, showing that the Al-Fe interface is free of the Al-Fe-Si layer and the aluminum alloy and the stainless steel were connected only by an O and Mg rich layer less than 10 nm in thickness at this location. Similar to the O and Mg rich layer in Fig. 6, the O and Mg rich layer in Fig. 7 can also be treated as a layer of the amorphous-crystalline nano-composite according to the bright field HR-STEM image and the corresponding FFT pattern (Fig. 7).

3.3. Interfacial bonding strength

The feasibility of producing novel interfacial microstructure at the Al-Fe interface using M-FSAM has been demonstrated by the investigation above. This section will show the resulting interfacial bonding strength of the bimetallic components made of 6061 aluminum alloy and 304 stainless steel using M-FSAM over a wide range of processing parameters.

Fig. 8a shows that high interfacial bonding strength between 6061 aluminum alloy and 304 stainless steel can be achieved over a wide range of tool traverse speeds from 0.3 m/min to 3 m/min. This is



Fig. 5. An illustration of the Al-Fe interfacial microstructure for further local analysis.

attractive for practical applications since a higher tool traverse speed offers the benefits of less machines and space, and reduced energy consumption for high volume production. Fig. 8a showed that the bimetallic components produced at 1000 rpm and 600 mm/min exhibited the highest nominal tensile strength of 280 MPa, which is close to the ultimate tensile strengths of the friction stir processed 6061 aluminum alloy. Liu and Ma (2008) have shown that the friction stir processed 6061 aluminum alloys have lower tensile strength than the 6061-T651 aluminum alloy due to the dissolution of Mg₂Si precipitates.

The fracture path of a representative Al-Fe miniature tensile specimen corresponding to 1000 rpm and 600 mm/min is shown in Fig. 8b, indicating the occurrence of a failure path within the aluminum alloy. Fractography of the miniature tensile specimens on the stainless steel side shows that the fracture surface can be divided into Region 1 and Region II (Fig. 8c). Region I is fully covered by a dimpled fracture of 6061 aluminum alloy, which is caused by a fracture of the aluminum alloys at about hundreds of micrometers away from the Al-Fe interface (Fig. 8b, c, and d). The majority of Region II was covered by a thin layer of dimpled fracture of 6061 aluminum alloy, and a few surface scratches carried over from the stainless steel under polished conditions were still observable. It can then be inferred that the presence of scratches on the original stainless steel surface created poor contact and friction conditions between the aluminum alloy and steel within the scratches, resulting in the formation of unbonded or weakly bonded regions around the scratches. The results imply that a smoother polished stainless steel surface prior to M-FSAM is necessary for promoting more homogenous friction between the aluminum alloy and steel along the interface and generating a homogeneously distributed nanoscale amorphous layer along the bonding interface, leading to enhanced bonding strength. It should be mentioned that the mirror finish of steel sheet can be achieved by the well-established practices in the industry and will not significantly increase the cost of the steel substrates, especially for high-volume production.

4. Discussion

4.1. Interfacial microstructure formation mechanism

Different from the Al-Fe bimetallic components produced by fusion-based manufacturing methods or E-FSAM in which the bonding interfaces are dominated by a continuous layer of IMCs, the interface of Al-Fe bimetallic components of 6061 aluminum alloy and 304 stainless steel produced by the M-FSAM was primarily characterized by the presence of nanoscale amorphous layer, which consisted of a continuous O and Mg rich layer (10–20 nm in thickness) and a discontinuous Al-Fe-Si layer (50–100 nm in thickness). The O and Mg rich layer was an amorphous-crystalline nano-composite while the Al-Fe-Si layer was characterized by hemispherical regions of an amorphous solid with some degree of crystallinity. Similarly, an O and Mg rich amorphous layer and discontinuous Al-Fe-Si amorphous layer were also observed at the interface of 6061 aluminum alloy and low carbon steel, but with a significantly reduced thickness (Liu et al., 2020).

Fig. 2f shows that the hemispherical Al-Fe-Si amorphous phase at the Al-Fe interface was separated by regions of fcc-Al matrix. Such a distribution is similar to that formed in the rapid solidified Al-Fe-Si alloy ribbons, in which nodules of nano-sized Al-Fe-Si amorphous phase separated by a matrix mainly consisting of pure fcc-Al with the Si inclusion particles as observed by Chapman et al. (2014). The Al-Fe-Si amorphous phase was characterized as a unique metallic glass

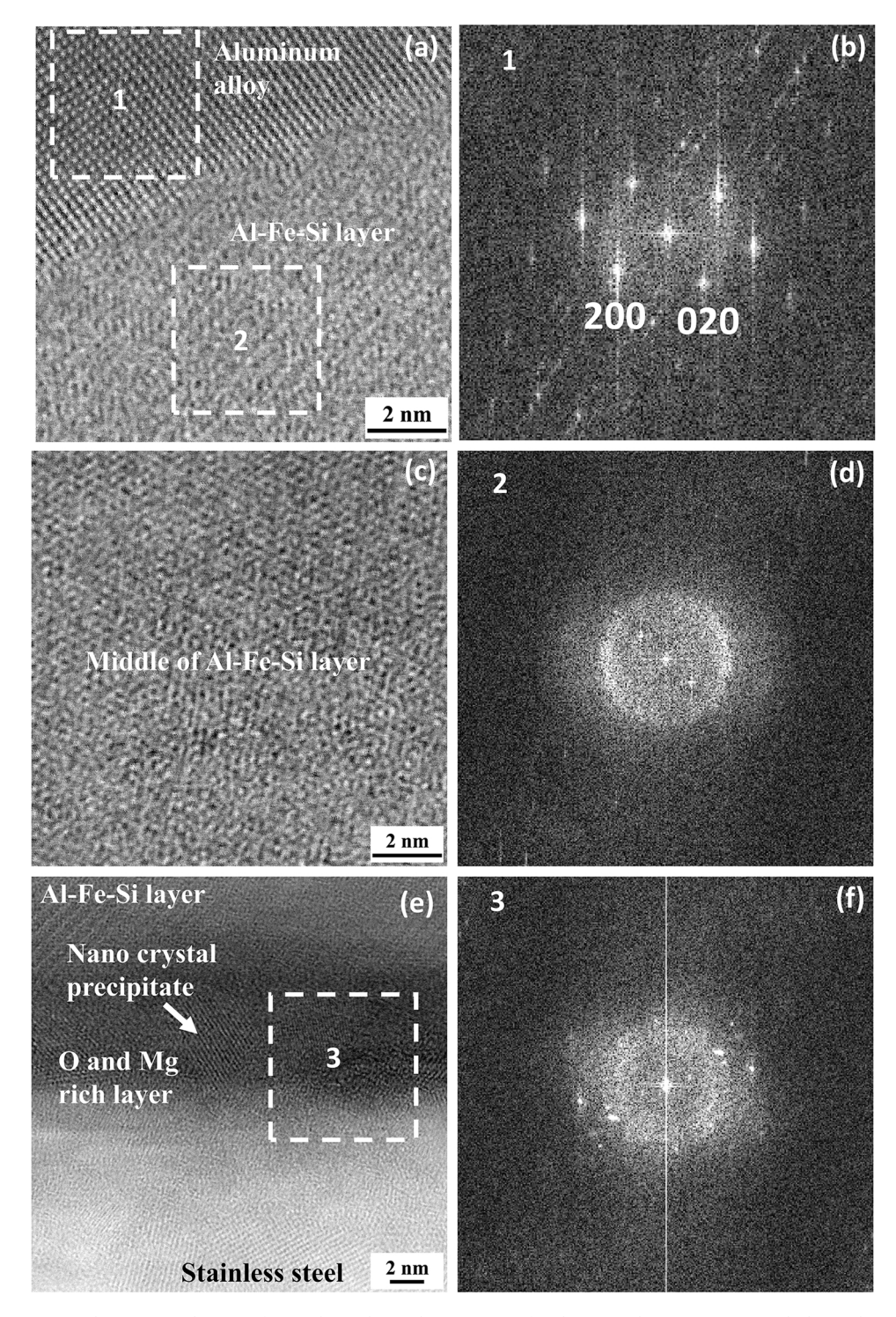


Fig. 6. HR-STEM BF imaging analysis across Al-Fe interface with an Al-Fe-Si layer: (a) interface between aluminum matrix and Al-Fe-Si layer, (c) middle of Al-Fe-Si layer, (e) O and Mg rich layer located between Al-Fe-Si layer and 304 stainless steel, and FFT pattern of (b) region 1, (d) region 2 and (f) region 3.

(so-called q-glass), which is neither a kinetically frozen liquid nor a polycrystalline aggregate of nanometer-sized crystalline grains but an atomically ordered, isotropic solid possessing no long-range translational symmetry (Long et al., 2013). The pair distribution function of the q-glass revealed the existence of chemical ordering that resembles that of cubic α Al-Fe-Si phase. Chapman et al. (2014) suggested that the q-glass grew from the melt by a first order phase transition similar to a crystalline solid via nucleation and growth.

Bendersky and Mompiou (2012) showed that after a rapid quenching of the $Al_{65}Fe_{15}Si_{20}$, $Al_{65}Ni_{15}Si_{20}$, $Al_{65}Ni_{10}Si_{20}$, and $Al_{65}Co_{10}Si_{20}$ melts

with an estimated cooling rate in the range of $2\text{--}3.5\times10^6$ K/s, different kinds of microstructure were obtained. A continuous major amorphous phase containing minor isolated nanocrystalline droplets formed in the $Al_{65}Ni_{15}Si_{20},\ Al_{65}Ni_{10}Si_{20},\ and\ Al_{65}Co_{10}Si_{20}$ ribbons. A microstructure similar to that of as-quenched $Al_{70}Fe_{13}Si_{17}$ (Cahn et al., 2003) formed in the as-quenched $Al_{65}Fe_{15}Si_{20}$ ribbon: nodules of q-glass and separating layers mainly consisting of well-orientated fcc-Al. Zigo et al. (2018) showed that the q-glass formed in $Al_{65}Fe_{15}Si_{20}$ alloy can persist at 305 °C for approximately 1 h with no significant change in microstructure while the metallic glass in $Al_{65}Ni_{15}Si_{20}$ transformed into fine

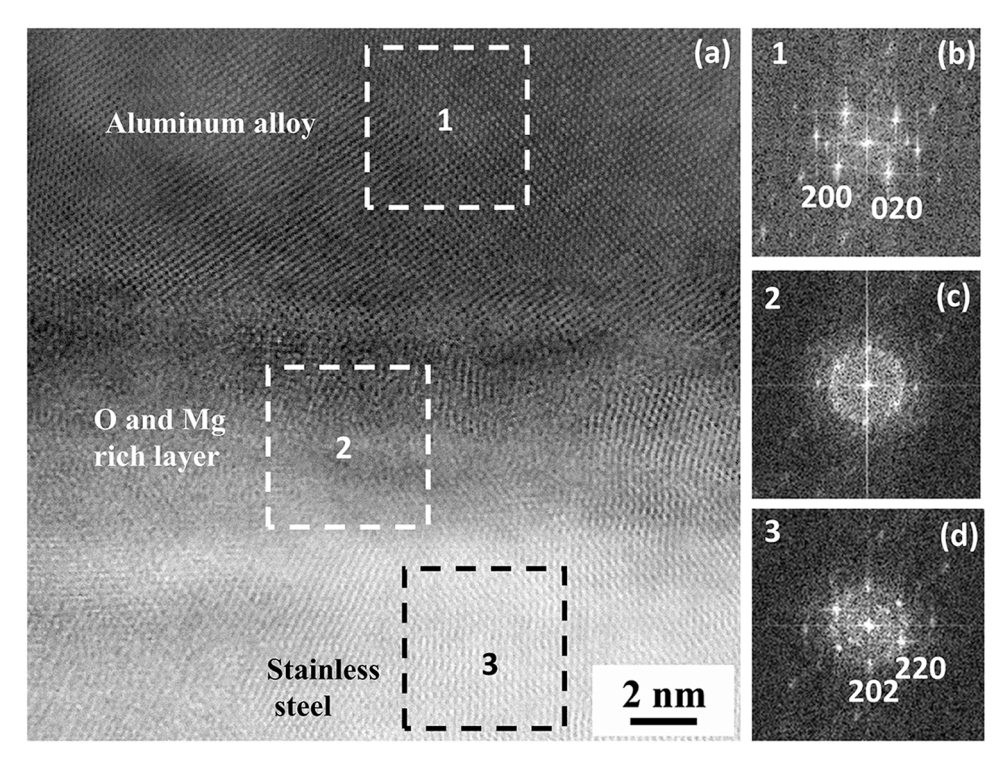


Fig. 7. HR-STEM analysis across Al-Fe interface at a location without Al-Fe-Si layer: (a) bright-field image and FFT patterns taken from (b) region 1, (c) region 2, and (d) region 3.

crystallines quickly at 245 °C. The difference in microstructure and thermal stability between the metallic glass of $Al_{65}Fe_{15}Si_{20}$ and $Al_{65}Ni_{15}Si_{20}$ ribbons suggested that the metallic glass in $Al_{65}Ni_{15}Si_{20}$ ribbon formed at a glass transition when atomic motion in a melt ceased while the q-glass in $Al_{65}Fe_{15}Si_{20}$ ribbon formed above the glass transition temperature by a first-order transition from the melt. Therefore, the q-glass is more stable at elevated temperatures.

Building upon the analysis above and the microstructure information of the hemispherical Al-Fe-Si amorphous particles collected in this study, it is reasonable to believe that the Al-Fe-Si amorphous phase formed at the Al-Fe interface should be classified as q-glass. Chapman et al. (2014) showed that a cooling rate higher than $10^6~{\rm K/s}$ is necessary for the formation of the q-glass in Al-Fe-Si alloy. However, Liu and Ma (2008) showed that the cooling rate during M-FSAM of 6061 aluminum alloy is lower than $10^2~{\rm K/s}$. Therefore, the formation of q-glass at the Al-Fe interface should not be ascribed to rapid quenching but to local premelting followed by highly localized shearing.

As illustrated in Fig. 9a, the rapid friction between the 6061 aluminum alloy and the 304 stainless steel triggered an interfacial premelting at the interface, leading to the formation of an undercooled liquid. As a result, the applied shear deformation was confined within the undercooled liquid layer, resulting in a shear localization. The average shear strain rate within the shear localization layer was higher than $10^6 \, \text{s}^{-1}$ during the M-FSAM under the condition that the relative friction speed between the steel and the aluminum alloy is around 0.4 m/s and the thickness of the undercooled liquid layer is 50-200 nm. The applied shear strain rate was so high that the atoms within the shear localization layer were unable to organize themselves into a fully ordered crystalline structure. The presence of undercooled liquid at the Al-Fe interface promoted the diffusion of solute atoms from surrounding aluminum alloys and stainless steels into the undercooled liquid, forming a layer of liquid aluminum alloy with a high concentration of specific alloying elements (e.g., Si and Fe) that produce the amorphous structure (Fig. 9b).

After the applied shear was removed or the shear rate was decreased to a level insufficient to maintain the homogenous elemental

distribution within the supercooled liquid, the supercooled liquid transformed into a two-phase solid: q-glass particles and fcc Al separating layer. Two possibilities were proposed for the formation of q-glass particles during this stage. The first one involves the mechanism put forward for q-glass in Al-Fe-Si alloys by Bendersky and Mompiou (2012). The q-glass particles formed directly from the undercooled liquid by nucleation and growth along with a moving interface between the solid and liquid (Fig. 9c). The q-glass has a definable solubility limit and rejected Al atoms during formation from the liquid. The other possibility is that the high degree of undercooling of the liquid led to an immiscibility gap between a solute lean aluminum liquid and a solute-rich aluminum liquid. In this case, a liquid phase separation reaction would take place after the applied shear strain rate was decreased and would lead to the formation of solute-rich aluminum droplets within the solute lean aluminum liquid (Fig. 9d). The q-glass then formed from the solute-rich aluminum droplets. More advanced experimental/simulation methods are required to clarify the formation mechanism of the interfacial microstructure.

It was observed that the content of Si in the Al-Fe-Si amorphous is about 7 wt%, which is much higher than the content of Si in the 6061 aluminum alloy (0.73 wt%) and 304 stainless steel (0.34 wt%) used in this study. Such a phenomenon can be ascribed to the diffusion of Si from aluminum alloys at elevated temperatures. Paccagnella et al. (1985) have calculated that Si can diffuse 7 μm in aluminum alloys for a cooling time of 10 s from 550° to 450°C. Liu and Ma (2008) showed that Si mainly exists as a high density of small needle- or rod-shaped Mg₂Si precipitates in 6061-T651 aluminum alloys. Fig. 10 shows that the majority of the Mg₂Si precipitates in 6061 aluminum alloys have dissolved into the aluminum matrix. A low density of spherical Si-rich precipitates was also observed in the aluminum alloys. A similar microstructure has been observed by Liu and Ma (2008) in friction stir welded 6061 aluminum alloy near the stir zone. The formation of such microstructure has been attributed to the dissolution of the precipitates at high temperatures during FSW.

The main alloying elements in the current 6061 aluminum alloy are Mg (1.1 wt%) and Si (0.73 wt%). Polmear and Sargant (1963) showed

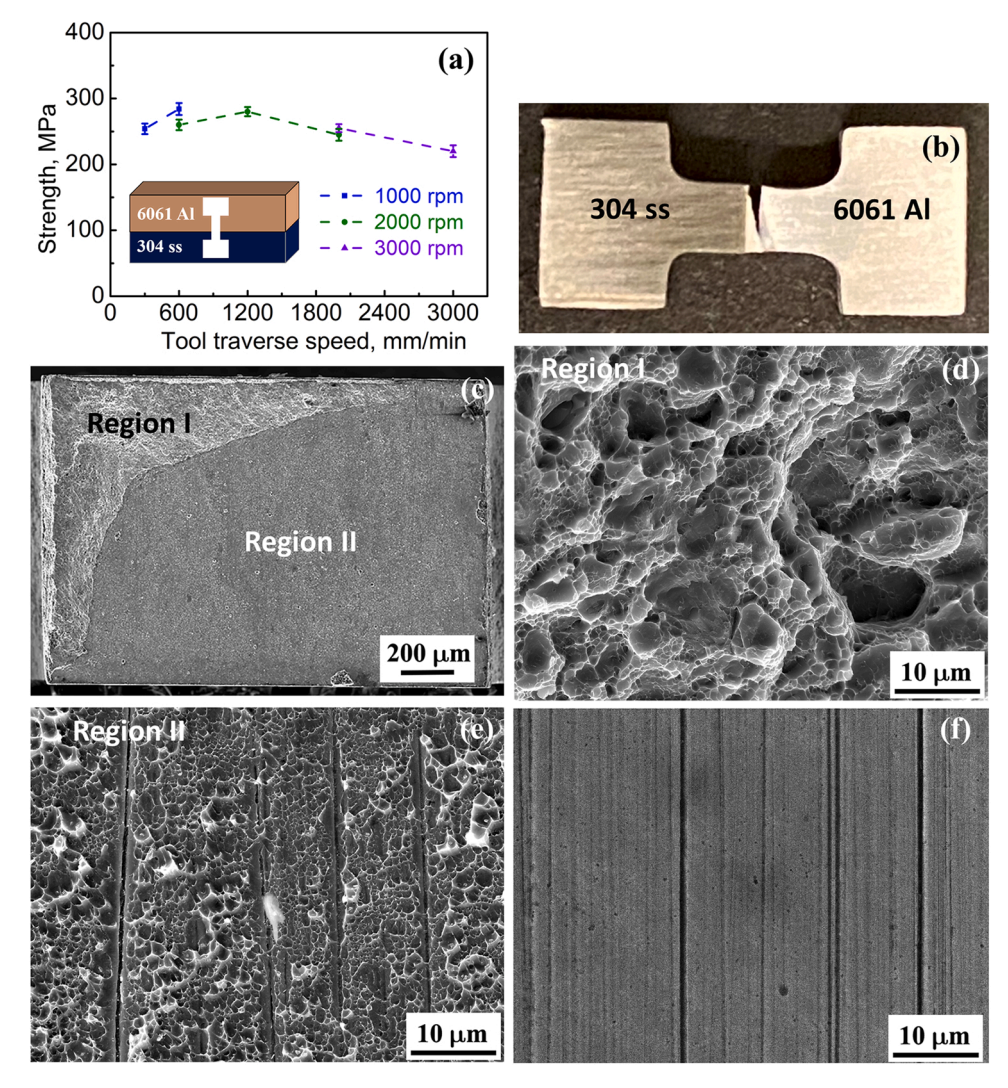


Fig. 8. (a) Effect of M-FSAM parameters on nominal tensile strength of bimetallic components of 6061 aluminum alloy and 304 stainless steel. A typical failed Al-Fe miniature tensile specimen produced by MFSAM at 1000 rpm and 600 mm/min: (c) low magnification electron backscatter image, (d) fracture surface of Region I in (c), (e) fracture surface of Region II in (c). (f) second electron (SE) image of polished 304 stainless steel with No. 8 mirror finish.

that the solubility of Mg in aluminum was > 15 wt% at 450 °C and decreased to ~ 1 wt% at room temperature while Fujikawa et al. (1979) showed that the solubility of Si in aluminum was 0.86 wt% at 500 °C and decreased to a few parts per million (ppm) at room temperature. The high temperature generated by M-FSAM can promote the rapid dissolution of Si and Mg elements into the 6061 aluminum alloy matrix. Bendersky and Mompiou (2012) showed that the solubility of Si in an Al-Fe-Si undercooled liquid can be higher than 20%, which is much higher than the solubility of Si in aluminum. This then promotes the diffusion of dissolved Si into the Al-Fe-Si undercooled liquid from the adjacent aluminum alloy. During the cooling stage of M-FSAM, part of the Si precipitated into Si-rich spherical particles while part of the Si was retained in solution in aluminum alloy matrix, forming a supersaturated solid solution due to the high cooling rate of M-FSAM. The analysis above was confirmed by the microstructure analysis in Fig. 10. Fig. 10f and g show that the content of Si solute in aluminum is much higher than the highest solubility of Si in aluminum at room temperature, demonstrating the formation of a supersaturated solid solution. Fig. 10g shows that the Si content in the aluminum alloy adjacent to the Al-Fe-Si layer is less than 0.4% and gradually increased to greater than 0.5% with an increase of the distance from the Al-Fe interface, which is direct evidence of the diffusion of Si from the aluminum alloy into the Al-Fe-Si layer. The low concentration gradient of Si in the aluminum alloy was attributed to the high diffusion rate of Si in aluminum at elevated temperatures.

The formation mechanism of the O and Mg rich layer is another area that needs to be investigated in the future. The current investigation showed that the distribution of the continuous O and Mg rich layer was not affected by the distribution of Al-Fe-Si particles. Therefore, the O and Mg rich layer should have formed and solidified before the formation of the Al-Fe-Si particles.

4.2. Significance in Al-Fe bimetallic component manufacturing

Compared to fusion-based welding or additive manufacturing methods, friction stir based welding and AM methods offer numerous advantages in the aspects of high bonding strength, process simplicity, and process automation. Therefore, an automotive company has adopted an FSW technique to produce Al-Fe bimetallic components (Kusuda, 2013). However, the adoption of the FSW for producing Al-Fe bimetallic components is still limited. This is because the Al-Fe bimetallic components produced by FSW often result in low bonding strength, high manufacturing cost, and low manufacturing throughput.

The existing FSW techniques require penetration of the stir probe into the steel for achieving an acceptable bonding strength (Wei et al., 2013). Since the steel needs to be stirred by a stir probe at elevated

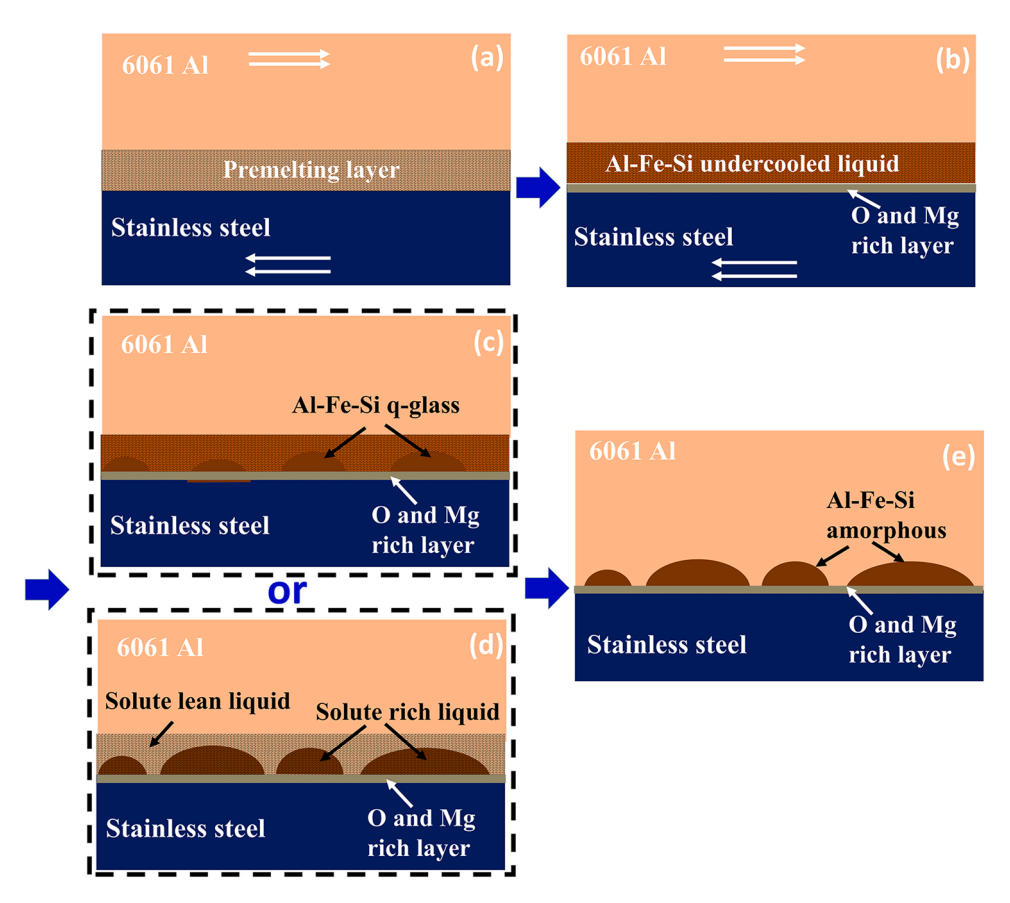


Fig. 9. A schematic illustration of the microstructure evolution at the interface of 6061 aluminum alloy and 304 stainless steel during an M-FSAM: (a) interfacial premelting caused by rapid friction, (b) alloying in the premelting layer due to atomic diffusion, (c) q-glass nucleation and growth, (d) liquid separation before solidification, and (e) final interfacial microstructure.

temperatures, expensive friction stir tools made from polycrystalline cubic boron nitride (PCBN) or tungsten-based alloys need to be used to have a reasonable tool life and constant joint quality (Wang et al., 2018). However, the operational lifetime of these tools is short and they must be frequently changed, resulting in a high tool cost per unit length of bonding. Since the stir probe does not need to penetrate the steel in the M-FSAM, inexpensive H13 tool steel is all that is needed for this new process. It should be noted that friction stir tools made of PCBN (Liu et al., 2018) or tungsten-based alloys can cost 10 times more than those made of H13 tool steels. In addition, the tool life of H13 stir tools for depositing aluminum alloys with this proposed process can be up to 10 times longer than that of the PCBN/ tungsten-based stir tools with the existing FSAM process. Therefore, the M-FSAM enables a potential reduction of the tool cost per unit length of Al-Fe bimetallic component of greater than 100 times compared to existing FSW/FSAM.

Due to the penetration of the probe into the steel, the tool rotation rate must be low enough to avoid heating the steel far above the melting point of the aluminum alloys (Wei et al., 2013). Correspondingly, a low tool traverse speed less than 300 mm/min needs to accommodate the low tool rotation rate to avoid the formation of void defects. Often, the tool traverse speed needs to be around 100 mm/min (Shamsujjoha et al., 2015). The current study showed that high tensile joint strength over 200 MPa has been achieved by M-FSAM at a high tool traverse speed of 3000 mm/min, which is 10 times higher than the tool traverse speed used in traditional FSW (Wei et al., 2013). What is more promising is that the bonding strength of the bimetallic components 6061 aluminum alloy and 304 stainless steel produced by the M-FSAM has reached 280 MPa which is close to the ultimate tensile strength of the 6061 aluminum alloy in the stir zone. In contrast, Wei et al. (2013) showed that the highest nominal shear joint strength of Al-Fe lap joints produced

by FSW is 89 MPa.

Although of M-FSAM Al-Fe bimetal structure offers advantages of higher interfacial bonding strength, lower cost, and reduced manufacturing procedures, it cannot produce components with complex shapes directly. M-FSAM may need to be integrated with a subtractive manufacturing method as a hybrid manufacturing process to produce components in the future. Since M-FSAM Al-Fe bimetal structures were mainly developed for producing large-sized components used as critical load-bearing structures, the requirement for shape complexity is relatively low compared to the small metal parts made by other AM processes.

5. Conclusions

- 1. This study showed that the novel modified friction stir additive manufacturing (M-FSAM) led to the formation of a nanoscale amorphous layer along the bonding interface between the 6061 aluminum alloy and 304 stainless steel by promoting interfacial premelting and localized alloy amorphization along the bonding interface. The high bonding strength of 280 MPa between the 6061 aluminum alloy and 304 stainless steel was achieved by the M-FSAM.
- 2. The nanoscale amorphous layer at the Al-Fe interface consisted of a continuous O and Mg rich layer 10–20 nm in thickness and a discontinuous Al-Fe-Si layer 50–100 nm in thickness. The O and Mg rich layer consisted of an amorphous matrix with nanocrystalline precipitates. The discontinuous Al-Fe-Si layer is comprised of hemispherical regions of amorphous q-glass with some degree of crystallinity.

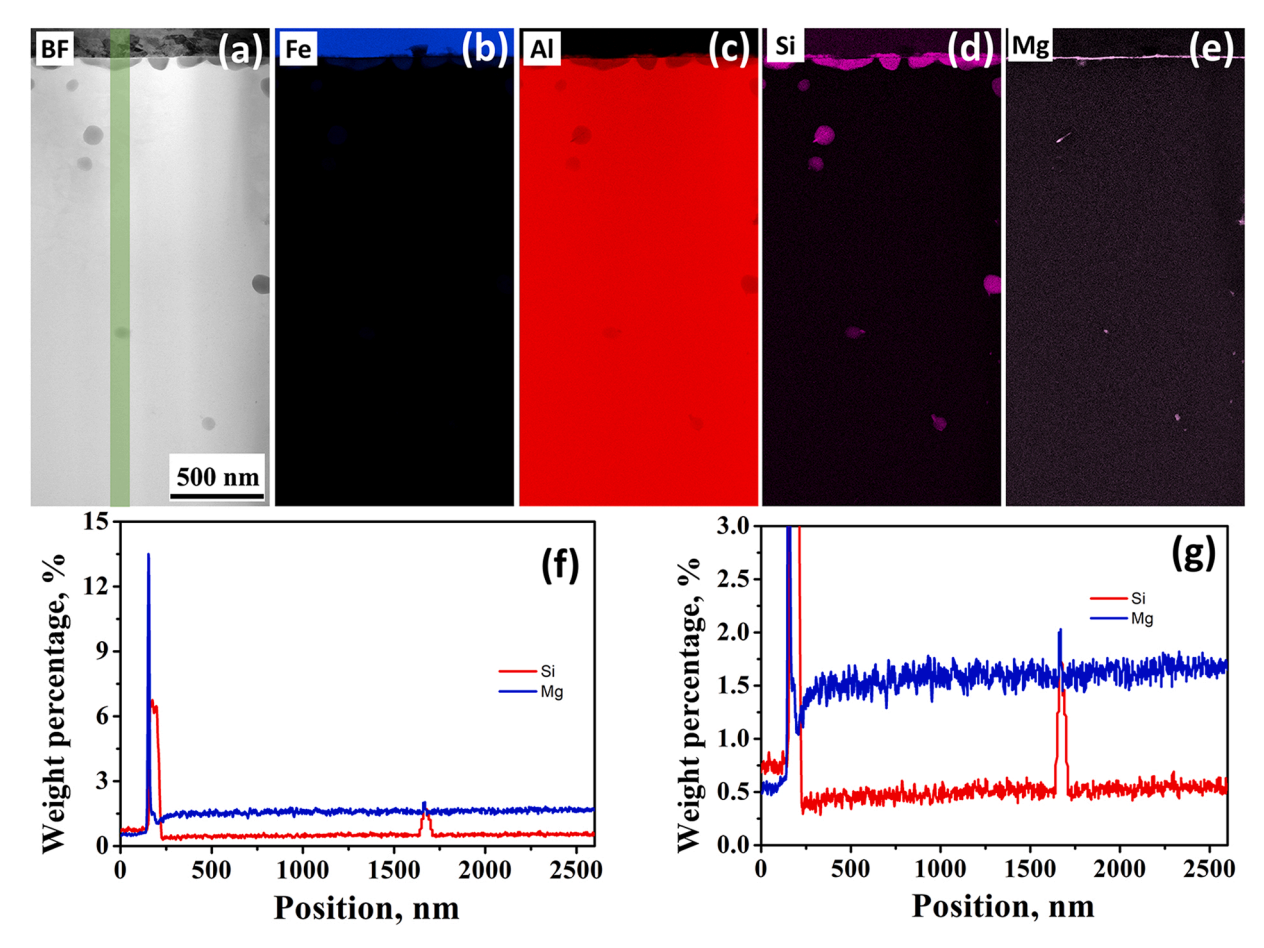


Fig. 10. Microstructure and element distribution from the bonding interface to the aluminum alloy matrix: (a) STEM-HAADF image; distribution of (b) Fe, (c) Al, (d) Si, and (e) Mg; (f) and (g) EDS line profiles obtained from the translucent green band in (a).

- 3. The content of Si in the Al-Fe-Si layer is about 7 wt%, which is much higher than the content of Si in the 6061 aluminum alloy and 304 stainless steel.
- 4. The M-FSAM was demonstrated to be a key enabler for producing Al-Fe bimetallic components of 6061 aluminum alloy and 304 stainless steel with bonding strength higher than 200 MPa over a wide range of tool traverse speeds (0.3–3 m/min) using a cost-effective tool made of H13 tool steel. Compared with the existing friction stir based methods, the M-FSAM showed its potential in producing stronger Al-Fe bimetallic components at significantly increased tool traverse speed and a remarkably reduced tool cost.

CRediT authorship contribution statement

F.C. Liu: Conceptualization, Investigation, Data curation, Methodology, Writing – original draft, Writing – review & editing. P. Dong: Conceptualization, Methodology, Funding acquisition, Resources, Supervision, Project administration, Writing – review & editing. A.S. Khan: Investigation, Writing – review & editing. K. Sun: Investigation, Writing – review & editing. W. Lu: Conceptualization, Resources, Supervision, Writing – review & editing. A. Taub: Conceptualization, Resources, Supervision, Writing – review & editing. J.E. Allison: Conceptualization, Resources, Supervision, Writing – review & editing.

Declaration of Competing Interest

The authors declare that they have no known competing financial interests or personal relationships that could have appeared to influence the work reported in this paper.

Data Availability

The authors confirm that the data supporting the findings of this study are available within the article. Raw data that support the findings of this study are available from the corresponding author, upon reasonable request.

Acknowledgments

This work was partially supported by the University of Michigan College of Engineering startup grant and the National Science Foundation (NSF CMMI 2126163). The authors acknowledge the financial support of the University of Michigan College of Engineering and technical support from the Michigan Center for Materials Characterization. The authors also acknowledge the support of C. R. T. N. Phanuphong on equipment operation and preparation of the test specimens.

References

Bendersky, L.A., Mompiou, F., 2012. Formation of Al-Fe-Si glass that grows from the melt through a first-order transition. J. Alloy. Compd. 536, S171–S174. https://doi. org/10.1016/j.jallcom.2012.01.056.

Cahn J.W., Bendersky L.A., 2003. An isotropic glass phase in Al-Fe-Si formed by a first order transition. MRS Online Proc. Libr., 806, pp. 126–130. (https://doi.org/10. 1557/PROC-806-MM2.7).

Cai, W., Daehn, G., Vivek, A., Li, J., Khan, H., Mishra, R.S., Komarasamy, M., 2019. A state-of-the-art review on solid-state metal joining. J. Manuf. Sci. Eng. 141 https://doi.org/10.1115/1.4041182.

Chapman, K.W., Chupas, P.J., Long, G.G., Bendersky, L.A., Levine, L.E., Mompiou, F., Stalick, J.K., Cahn, J.W., 2014. An ordered metallic glass solid solution phase that grows from the melt like a crystal. Acta Mater. 62, 58–68. https://doi.org/10.1016/j. actamat.2013.08.063.

- Fujikawa, S., Oyobiki, Y., Hirano, K., 1979. Studies on solid solubility of silicon in aluminum and ostwald ripening of silicon precipitates in Al–Si alloys by means of electrical resistivity measurement. J. Jpn. Inst. Met. 29, 331–339. https://doi.org/ 10.2464/jilm.29.331
- Kusuda, Y., 2013. Honda develops robotized FSW technology to weld steel and aluminum and applied it to a mass-production vehicle. Ind. Robot Int. J. 40, 208–212. https://doi.org/10.1108/01439911311309889.
- Liu, F.C., Dong, P., 2021. From thick intermetallic to nanoscale amorphous phase at Al-Fe joint interface: roles of friction stir welding conditions. Scr. Mater. 191, 167–172. https://doi.org/10.1016/j.scriptamat.2020.09.031.
- Liu, F.C., Ma, Z.Y., 2008. Influence of tool dimension and welding parameters on microstructure and mechanical properties of friction-stir-welded 6061-T651 aluminum alloy. Metall. Mater. Trans. A 39, 2378–2388. https://doi.org/10.1007/ s11661-008-9586-2.
- Liu, F.C., Hovanski, Y., Miles, M.P., Sorensen, C.D., Nelson, T.W., 2018. A review of friction stir welding of steels: tool, material flow, microstructure, and properties. J. Mater. Sci. Technol. 34, 39–57. https://doi.org/10.1016/j.jmst.2017.10.024.
- Liu, F.C., Dong, P., Zhang, J., Lu, W., Taub, A., Sun, K., 2020. Alloy amorphization through nanoscale shear localization at Al-Fe interface. Mater. Today Phys. 15, 100252 https://doi.org/10.1016/j.mtphys.2020.100252.
- Liu, J., Hao, Z., Xie, Y., Meng, X., Huang, Y., Wan, L., 2022. Interface stability and fracture mechanism of Al/Steel friction stir lap joints by novel designed tool. J. Mater. Process. Technol. 300, 117425 https://doi.org/10.1016/j. imatprotec.2021.117425.
- Long, G.G., Chapman, K.W., Chupas, P.J., Bendersky, L.A., Levine, L.E., Mompiou, F., Stalick, J.K., Cahn, J.W., 2013. Highly ordered noncrystalline metallic phase. Phys. Rev. Lett. 111, 15502. https://doi.org/10.1103/PhysRevLett.111.015502.
- Paccagnella, A., Ottaviani, G., Fabbri, P., Ferla, G., Queirolo, G., 1985. Silicon diffusion in aluminium. Thin Solid Films 128, 217–223. https://doi.org/10.1016/0040-6090 (85)90073-2.
- Palanivel, S., Nelaturu, P., Glass, B., Mishra, R.S., 2015. Friction stir additive manufacturing for high structural performance through microstructural control in an Mg based WE43 alloy. Mater. Des. 65, 934–952. https://doi.org/10.1016/j. matdes.2014.09.082.
- Polmear, I.J., Sargant, K.R., 1963. Enhanced age-hardening in aluminium–magnesium alloys. Nature 200, 669–670. https://doi.org/10.1038/200669b0.

- Sames, W.J., List, F.A., Pannala, S., Dehoff, R.R., Babu, S.S., 2016. The metallurgy and processing science of metal additive manufacturing. Int. Mater. Rev. 61, 315–360. https://doi.org/10.1080/09506608.2015.1116649.
- Shamsujjoha, M., Jasthi, B.K., West, M., Widener, C., 2015. Friction stir lap welding of aluminum to steel using refractory metal pin tools. J. Eng. Mater. Technol. 137, 021009 https://doi.org/10.1115/1.4029571.
- Wang, T., Sidhar, H., Mishra, R.S., Hovanski, Y., Upadhyay, P., Carlson, B., 2018. Friction stir scribe welding technique for dissimilar joining of aluminium and galvanised steel. Sci. Technol. Weld. Join. 23, 249–255. https://doi.org/10.1080/ 13621718.2017.1381460.
- Wang, T., Sidhar, H., Mishra, R.S., Hovanski, Y., Upadhyay, P., Carlson, B., 2019. Evaluation of intermetallic compound layer at aluminum/steel interface joined by friction stir scribe technology. Mater. Des. 174, 107795 https://doi.org/10.1016/j. matdes.2019.107795.
- Watanabe, T., Takayama, H., Yanagisawa, A., 2006. Joining of aluminum alloy to steel by friction stir welding. J. Mater. Process. Technol. 178, 342–349. https://doi.org/ 10.1016/j.jmatprotec.2006.04.117.
- Wei, Y., Li, J., Xiong, J., Zhang, F., 2013. Effect of tool pin insertion depth on friction stir lap welding of aluminum to stainless steel. J. Mater. Eng. Perform. 22, 3005–3013. https://doi.org/10.1007/s11665-013-0595-y.
- Yu, H.Z., Mishra, R.S., 2021. Additive friction stir deposition: a deformation processing route to metal additive manufacturing. Mater. Res. Lett. 9, 71–83. https://doi.org/ 10.1080/21663831.2020.1847211.
- Zhang, Y., Bandyopadhyay, A., 2021. Influence of compositionally graded interface on microstructure and compressive deformation of 316L stainless steel to Al12Si aluminum alloy bimetallic structures. ACS Appl. Mater. Interfaces 13, 9174–9185. https://doi.org/10.1021/acsami.0c21478.
- Zhou, L., Yu, M., Liu, B., Zhang, Z., Liu, S., Song, X., Zhao, H., 2020. Microstructure and mechanical properties of Al/steel dissimilar welds fabricated by friction surfacing assisted friction stir lap welding. J. Mater. Res. Technol. 9, 212–221. https://doi. org/10.1016/j.jmrt.2019.10.046.
- Zigo, J., Roik, O., Švec, P., Mihalkovic, M., Švec, P., Mačko, I., 2018. Study of the Al-T-Si (T=Fe, Co, Ni) alloys in the solid, liquid and as-quenched states. Mater. Charact. 138, 315–324. https://doi.org/10.1016/j.matchar.2017.11.044.